

PAPER • OPEN ACCESS

Magnetic induction tomography via the monotonicity principle

To cite this article: Gianpaolo Piscitelli *et al* 2023 *J. Phys.: Conf. Ser.* **2444** 012005

View the [article online](#) for updates and enhancements.

You may also like

- [Monotonicity-based electrical impedance tomography for lung imaging](#)
Liangdong Zhou, Bastian Harrach and Jin Keun Seo
- [Remarks on the factorization and monotonicity method for inverse acoustic scatterings](#)
Takashi Furuya
- [Monotonicity of a quantum 2-Wasserstein distance](#)
R Bistro, M Eckstein and K yczkowski



245th ECS Meeting
San Francisco, CA
May 26–30, 2024

PRiME 2024
Honolulu, Hawaii
October 6–11, 2024

Bringing together industry, researchers, and government across 50 symposia in electrochemistry and solid state science and technology

Learn more about ECS Meetings at
<http://www.electrochem.org/upcoming-meetings>

 Save the Dates for future ECS Meetings!

Magnetic induction tomography via the monotonicity principle

Gianpaolo Piscitelli¹, Zhiyi Su², Lalita Udpa³, Antonello Tamburrino^{3,4,*}

¹ Dipartimento di Matematica e Applicazioni “R. Caccioppoli”, Università degli Studi di Napoli Federico II, Via Cinthia n. 26, Complesso Universitario Monte Sant’Angelo, 81026 Napoli, Italy

² Zhejiang Lab, Hangzhou, Zhejiang 311121, China

³ Department of Electrical and Computer Engineering, Michigan State University, East Lansing, MI-48824, USA

⁴ Dipartimento di Ingegneria Elettrica e dell’Informazione “M. Scarano”, Università degli Studi di Cassino e del Lazio Meridionale, Via G. Di Biasio n. 43, 03043 Cassino (FR), Italy

E-mail: gianpaolo.piscitelli@unina.it; suzy@zhejianglab.com; udpal@egr.msu.edu; antonello.tamburrino@unicas.it

Abstract. This contribution is focused on the nonlinear and ill-posed problem of reconstructing the electrical conductivity starting from the free response of a conductor in the magneto-quasi-stationary (MQS) limit. In this framework, a key role is played by the Monotonicity Principle, that is a monotone relation connecting the unknown material property to the (measured) free-response. The Monotonicity Principle is relevant to develop noniterative and real-time imaging methods. The Monotonicity Principle is a rather general principle found in many different physical problems. However, each physical/mathematical context requires the proper operator showing the MP to be identified. In turns, this calls for ad-hoc mathematical approaches tailored to the specific frameworks. In this paper we discuss a monotonic relationship between the electrical resistivity and the time constants of the free response for MQS systems. Numerical examples are provided to support the underlying theory.

1. Introduction

In this article, which is derived from [1, 2, 3, 4], we analyze the inverse problem of reconstructing the electrical conductivity from the free response of Maxwell equations in the magneto-quasi-stationary (MQS) limit. In this limiting case fall the phenomena in which (i) the displacement current appearing in the Ampère-Maxwell law can be neglected, (ii) there is a conducting material and (iii) the magnetic energy of the system

* Author to whom any correspondence should be addressed. ORCID: 0000-0003-2462-6350.



dominates the electrical energy [5]. The time-varying magnetic flux density in the MQS limit is able to penetrate inside a conducting material inducing electrical currents and it is known as eddy currents. In turn, the magnetic flux density, produced by the induced eddy currents, can be measured using sensors external to the conductor, thus enabling the tomographic capabilities (Eddy Current Tomography or Magneto Inductive Tomography) of material properties, such as the electrical resistivity (or, equivalently, conductivity) and magnetic permeability. Specifically, in this work we refer to the response of the system when all sources have been switched off as the imaging of a conductor's electrical conductivity starting from the free response of the material. We do not assume magnetic properties for the conducting material, but, however, the extension to conductive and magnetic materials is straightforward.

Several models have been studied for Eddy Currents. Here we choose the following integral formulation (non-magnetic materials) to study the free response on an Eddy Current problem [6]:

$$\langle \eta \mathbf{J}, \mathbf{w} \rangle = -\partial_t \langle A \mathbf{J}, \mathbf{w} \rangle \quad \forall \mathbf{w} \in H_L(\Omega),$$

where \mathbf{J} is the induced current density, Ω is the region occupied by the conducting material, A is the compact, self-adjoint, positive definite operator:

$$A : \mathbf{v} \in H_L(\Omega) \mapsto \frac{\mu_0}{4\pi} \int_{\Omega} \frac{\mathbf{v}(x')}{\|x - x'\|} dV(x') \in L^2(\Omega; \mathbb{R}^3), \quad (1.1)$$

$H_L(\Omega)$ is the functional space

$$H_L(\Omega) := \{ \mathbf{v} \in H_{\text{div}}(\Omega) \mid \text{div}(\mathbf{v}) = 0 \text{ in } \Omega, \mathbf{v} \cdot \hat{\mathbf{n}} = 0 \text{ on } \partial\Omega \},$$

η is the electrical resistivity and μ_0 is free space magnetic permeability.

The Monotonicity Principle (MP) plays a key role in inverse problems; it is based on a monotonic relationship connecting the unknown material property to the measured physical quantity. The MP is fundamental for developing non-iterative imaging methods suitable for real-time imaging. It was introduced by A. Tamburrino and G. Rubinacci in [7, 8, 9] and it has mainly been applied to inverse obstacle problems. In these framework, the aim is to reconstruct the shape of defects in a given background and the method determines whether or not a test inclusion is part of an defect. This test is highly suitable for three main features: (i) the negligible computational cost for processing a given test inclusion, (ii) the processing on different test inclusions can be carried out in parallel, and (iii) the MP provides rigorous upper and lower bounds to the unknown defect, even in the presence of noise (see [10] and references therein), under proper assumptions. Subsequently, the MP was extended to many different settings [2, 1, 11, 12, 13, 4, 14, 15, 16, 17, 18, 19, 20, 21]) and even to nonlinear materials [22].

The class of non-iterative imaging methods also includes the imaging methods based on the MP. Colton and Kirsch introduced the first non-iterative approach named Linear Sampling Method (LSM) [23], then Kirsch proposed the Factorization Method (FM) [24]. Ikeata proposed the Enclosure Method [25] and Devaney applied MUSIC (MUltiple Signal Classification), a well-known algorithm in signal processing, as an imaging method

[26]. In [27], a non-iterative method based on the concept of topological derivatives is proposed to find the shape of defects in an otherwise homogeneous material.

In this article, we prove that the electrical current density in the absence of the source (source-free response) can be represented through a modal decomposition:

$$\mathbf{J}(x, t) = \sum_{n=1}^{\infty} c_n \mathbf{j}_n(x) e^{-t/\tau_n(\eta)} \quad \text{in } \Omega \times [0, +\infty[. \quad (1.2)$$

In modal decomposition (1.2), $\mathbf{j}_n(x)$ is a mode and $\tau_n(\eta) > 0$ is the corresponding time constant, $\forall n \in \mathbb{N}$. Each mode and its related time constant depend on the electrical resistivity η . In Proposition 2.1 we prove that the sequence of modes $\{\mathbf{j}_n\}_{n \in \mathbb{N}}$ is a complete basis. Moreover, we prove that $\tau_n(\eta) \rightarrow 0$ as $n \rightarrow \infty$. Equation (1.2) allows us to generalize the representation in [2, eq. (20)], valid for the discrete case, to the continuous case.

Moreover, in Theorem 3.3, we prove the MP for the sequence of time constants $\{\tau_n(\eta)\}_{n \in \mathbb{N}}$:

$$\eta_1 \leq \eta_2 \quad \Rightarrow \quad \tau_n(\eta_1) \geq \tau_n(\eta_2) \quad \forall n \in \mathbb{N}, \quad (1.3)$$

where $\eta_1 \leq \eta_2$ means $\eta_1(x) \leq \eta_2(x)$ for a.e. $x \in \Omega$. The time constants $\tau_n(\eta)$ appearing in (1.3) must be ordered monotonically. Hereafter, we assume they are placed in decreasing order.

The paper is organized as follows. In Section 2, we describe the inverse problem of interest, together with the mathematical model of the underlying physics. In Section 3, we prove the MP for time constants. In Section 4 we provide a discussion of the results together with the imaging method and in Section 5 we provide some numerical examples.

2. Statement of the Problem

The model problem in Magnetic Induction Tomography (MIT) consists in studying the electromagnetic fields to retrieve the spatial distribution of the electrical resistivity of a prescribed material.

The time-varying electrical currents, that circulate in a proper set of coils (see Figure 1), generate an electromagnetic field. The time-varying currents produce a time-varying magnetic flux density $\mathbf{B}(x, t)$ that induces an electrical field $\mathbf{E}(x, t)$ and, consequently, an electrical current density $\mathbf{J}(x, t)$ in the conducting domain Ω [5]. The electrical resistivity η affects the induced current density $\mathbf{J}(x, t)$ which, in turns, produces a “reaction” magnetic flux density $\mathbf{B}^{eddy}(x, t)$. In MIT the measurement of $\mathbf{B}^{eddy}(x, t)$ carried out externally to the conducting domain, makes it possible, in principle, to reconstruct the unknown η .

Two types of measurements are related to \mathbf{B}^{eddy} . The first one consists in measuring \mathbf{B}^{eddy} with a magnetic flux density sensor, the second consists in measuring the induced voltage $v_{eddy}(t)$ across a pick-up coil. It is worth noting that $v^{eddy} = d\varphi^{eddy}/dt$ where φ^{eddy} is the magnetic flux linked with the pick-up coil. Furthermore, these quantities share the same set of time constants of \mathbf{J} . Indeed, the applications of the Biot-Savart

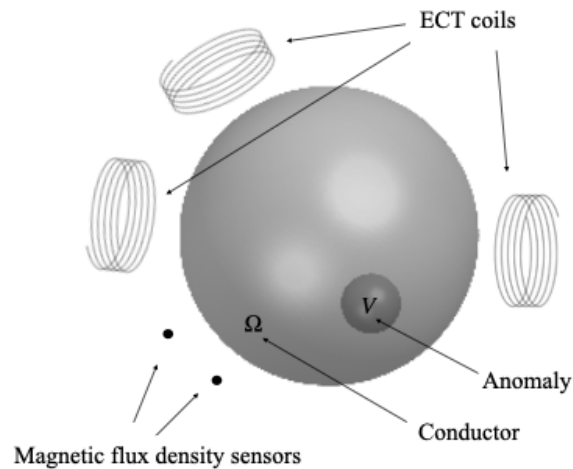


Figure 1. Representation of a typical Magnetic induction tomography. This Figure is reproduced from [1] with the kind permission of Institute of Physics (IOP).

law to the source free response (1.2) yields to:

$$\mathbf{B}^{eddy}(x, t) = \sum_{n=1}^{\infty} c_n \mathbf{b}_n(x) e^{-t/\tau_n(\eta)} \quad \text{in } \Omega \times [0, +\infty[, \quad (2.1)$$

$$v^{eddy}(t) = \frac{d\varphi^{eddy}(t)}{dt} = \sum_{n=1}^{\infty} c_n v_n e^{-t/\tau_n(\eta)} \quad \text{in } \Omega \times [0, +\infty[. \quad (2.2)$$

Therefore, the protocol entails in gathering the waveform of either \mathbf{B}^{eddy} or v^{eddy} . Hence, the waveforms are pre-processed to extract the time constants and, finally, the set of time constants is provided as input to the imaging algorithm.

Throughout this paper, Ω is the region occupied by the conducting material. We assume $\Omega \subset \mathbb{R}^3$ to be an open bounded domain with a Lipschitz boundary and outer unit normal $\hat{\mathbf{n}}$. We denote by V and S the 3-dimensional and the bi-dimensional Hausdorff measure in \mathbb{R}^3 , respectively and by $\langle \cdot, \cdot \rangle$ the usual L^2 -integral product on Ω .

Hereafter we refer to the following functional spaces

$$L_+^\infty(\Omega) := \{\theta \in L^\infty(\Omega) \mid \theta \geq c_0 \text{ a.e. in } \Omega \text{ for } c_0 > 0\},$$

and to the derived spaces $L^2(0, T; H_L(\Omega))$ and $L^2(0, T; H_{\text{curl}}(\Omega))$, for any $0 < T < +\infty$.

Let \mathbf{E} , \mathbf{B} , \mathbf{H} and \mathbf{J} be the electric field, the magnetic flux density, the magnetic field and the electrical current density, respectively where $\eta \in L_+^\infty(\Omega)$ is the electrical resistivity of the conductor, μ_0 is the magnetic permeability of the free space, \mathbf{J}_s is the prescribed source current density and we have assumed that there are no magnetic materials. The Magneto-Quasi-Stationary approximation of Maxwell's equations is

described by (see, for instance, [28]) in integral formulation in the weak form (see [29, 6]) by:

$$\langle \eta \mathbf{J}, \mathbf{w} \rangle = -\langle \partial_t A \mathbf{J}, \mathbf{w} \rangle - \langle \partial_t \mathbf{A}_S, \mathbf{w} \rangle \quad \forall \mathbf{w} \in H_L(\Omega), \quad (2.3)$$

where $\mathbf{A}_S \in L^2(0, T; H_{\text{curl}}(\Omega))$ is the vector potential produced by the prescribed source current $\mathbf{J}_s \in L^2(0, T; H_L(\Omega_s))$, Ω_s is a bounded open set with Lipschitz boundary, A is the operator defined in (1.1) and $\mathbf{J} \in L^2(0, T; H_L(\Omega))$.

This Section provides the characterization of the time constants. Specifically, it has been found that the time constants are the eigenvalues for a proper generalized eigenvalue problem [1]. To find this generalized eigenvalue problem, we notice that in the absence of source currents (2.3) reduces to:

$$\langle \eta \mathbf{J}, \mathbf{w} \rangle = -\partial_t \langle A \mathbf{J}, \mathbf{w} \rangle \quad \forall \mathbf{w} \in H_L(\Omega).$$

Then, the separation of variables $\mathbf{J}(x, t) = i(t) \mathbf{j}(x)$ gives

$$i(t) \langle \eta(x) \mathbf{j}(x), \mathbf{w}(x) \rangle = -i'(t) \langle A \mathbf{j}(x), \mathbf{w}(x) \rangle \quad \forall \mathbf{w} \in H_L(\Omega),$$

and, therefore,

$$\begin{aligned} \frac{i(t)}{i'(t)} &= -\tau(\eta) \quad \forall t \in]0, +\infty[, \\ \frac{\langle A \mathbf{j}, \mathbf{w} \rangle}{\langle \eta \mathbf{j}, \mathbf{w} \rangle} &= \tau(\eta) \quad \forall \mathbf{w} \in H_L(\Omega), \end{aligned}$$

where $\tau(\eta)$ is the separation constant. Therefore, $\mathbf{J}(x, t) = e^{-t/\tau(\eta)} \mathbf{j}(x)$ and

$$\langle A \mathbf{j}, \mathbf{w} \rangle = \tau(\eta) \langle \eta \mathbf{j}, \mathbf{w} \rangle \quad \forall \mathbf{w} \in H_L(\Omega). \quad (2.4)$$

When (2.4) admits a nonzero solution, the real number τ and the function $\mathbf{j} \in H_L(\Omega) \setminus \{\mathbf{0}\}$ are called the *eigenvalue* and *eigenfunction* of (2.4), respectively.

In [1] it has been proved that:

- (i) the generalized eigenvalues and eigenvectors form countable sets: $\{\tau_n(\eta)\}_{n \in \mathbb{N}}$ and $\{\mathbf{j}_n\}_{n \in \mathbb{N}}$;
- (ii) the eigenvalues can be ordered such that $\tau_n(\eta) \geq \tau_{n+1}(\eta)$;
- (iii) $\tau_n(\eta) > 0$ and $\lim_{n \rightarrow +\infty} \tau_n(\eta) = 0$;
- (iv) the set of eigenvectors $\{\mathbf{j}_n\}_{n \in \mathbb{N}}$ forms a complete basis in $H_L(\Omega)$.

We stress that the sequence $\{\mathbf{j}_n\}_{n \in \mathbb{N}}$ form a complete basis, hence it can be used to represent any element of $H_L(\Omega)$ in terms of a Fourier series.

Furthermore, by induction, we define

$$\tau_n(\eta) := \max_{\|\mathbf{j}\|_\eta=1, \mathbf{j} \in H_L^n(\Omega)} \langle A \mathbf{j}, \mathbf{j} \rangle \quad n = 1, 2, \dots \quad (2.5)$$

where

$$\begin{aligned} H_L^1(\Omega) &:= H_L(\Omega) \\ H_L^n(\Omega) &:= \{\mathbf{v} \in H_L(\Omega) \mid \langle \mathbf{v}, \eta \mathbf{j}_1 \rangle = \dots = \langle \mathbf{v}, \eta \mathbf{j}_{n-1} \rangle = 0\} \quad n = 2, 3, \dots \end{aligned}$$

Proposition 2.1. *The sequence $\{\mathbf{j}_n\}_{n \in \mathbb{N}}$ of the maximizers of (2.5) forms a complete basis in $H_L(\Omega)$.*

Proof. Let us assume that there exists $\mathbf{v} \in H_L(\Omega) \setminus \text{span}\{\mathbf{j}_n\}_{n \in \mathbb{N}}$. Let us decompose \mathbf{v} as $\mathbf{v} = \mathbf{v}_1 + \mathbf{v}_2$ with $\mathbf{v}_1 \in \text{span}\{\mathbf{j}_n\}_{n \in \mathbb{N}}$ and $\mathbf{v}_2 \neq \mathbf{0}$ such that $\langle \mathbf{v}_2, \eta \mathbf{j}_n \rangle = 0, \forall n \in \mathbb{N}$. Thanks to the latter, $\mathbf{v}_2 \in H_L^n(\Omega) \forall n \in \mathbb{N}$, thus

$$\tau_n = \sup_{\|\mathbf{v}\|_\eta=1, \mathbf{v} \in H_L^n(\Omega)} \langle A\mathbf{v}, \mathbf{v} \rangle \geq \left\langle A \frac{\mathbf{v}_2}{\|\mathbf{v}_2\|_\eta}, \frac{\mathbf{v}_2}{\|\mathbf{v}_2\|_\eta} \right\rangle > 0$$

where the last inequality comes from the positive definiteness of A . In the limits for $n \rightarrow +\infty$ we get $0 > 0$ which is a contradiction. Thus, $\mathbf{v}_2 = \mathbf{0}$, i.e. $\{\mathbf{j}_n\}_{n \in \mathbb{N}}$ is complete basis in $H_L(\Omega)$. \square

3. Monotonicity of eigenvalues

This Section provides the proof of the MP for the time constants. To achieve this aim, we first derive a variational characterization of the time constants in a slightly different form with respect to (2.5). More precisely, this new variational characterization (3.2) have two specific features: (i) it involves a finite dimensional space, rather than an infinite dimensional space and (ii) the set of admissible functions does not depend upon the electrical resistivity η . The first result is contained in Lemma 3.1 whereas the second result is in Lemma 3.2.

3.1. Variational Characterization

We have the two following variation characterizations of the eigenvalues [1].

Lemma 3.1. *The following variational characterization of $\tau_n(\eta)$ holds:*

$$\tau_n(\eta) = \min_{\mathbf{j} \in U_n} \frac{\langle A\mathbf{j}, \mathbf{j} \rangle}{\|\mathbf{j}\|_\eta^2}, \quad (3.1)$$

where $U_n = \text{span}\{\mathbf{j}_1, \mathbf{j}_2, \dots, \mathbf{j}_n\}$

Lemma 3.2. *The following max-min variational characterization of $\tau_n(\eta)$ holds:*

$$\tau_n(\eta) = \max_{\dim(U)=n} \min_{\mathbf{j} \in U} \frac{\langle A\mathbf{j}, \mathbf{j} \rangle}{\|\mathbf{j}\|_\eta^2}. \quad (3.2)$$

3.2. The Monotonicity Principle for the Eigenvalues

At this stage, we are in position to prove the main result of this paper, i.e. the Monotonicity of the time constants with respect to the electrical resistivity η . We stress that a key role is played by the variational characterization (3.2) appearing in Lemma 3.2.

Theorem 3.3. *Let $\eta_1, \eta_2 \in L_+^\infty(\Omega)$. It holds that*

$$\eta_1 \leq \eta_2 \text{ a.e. in } \Omega \implies \tau_n(\eta_1) \geq \tau_n(\eta_2) \quad \forall n \in \mathbb{N},$$

$\tau_n(\eta_1)$ being the n -th eigenvalue related to η_1 and $\tau_n(\eta_2)$ the one related to η_2 .

Proof. First, we observe that if $\eta_1 \leq \eta_2$ a.e. in Ω , then $\|\mathbf{v}\|_{\eta_1}^2 = \langle \eta_1 \mathbf{v}, \mathbf{v} \rangle \leq \langle \eta_2 \mathbf{v}, \mathbf{v} \rangle \leq \|\mathbf{v}\|_{\eta_2}$. Then, $\langle A\mathbf{v}, \mathbf{v} \rangle / \|\mathbf{v}\|_{\eta_1} \langle A\mathbf{v}, \mathbf{v} \rangle / \|\mathbf{v}\|_{\eta_2}$ and

$$\min_{\mathbf{v} \in U} \frac{\langle A\mathbf{v}, \mathbf{v} \rangle}{\|\mathbf{v}\|_{\eta_1}} \geq \min_{\mathbf{v} \in U} \frac{\langle A\mathbf{v}, \mathbf{v} \rangle}{\|\mathbf{v}\|_{\eta_2}},$$

where U is a linear space. Eventually, from Lemma 3.2, we have

$$\tau_n(\eta_1) = \max_{\dim(U)=n} \min_{\mathbf{v} \in U} \frac{\langle A\mathbf{v}, \mathbf{v} \rangle}{\|\mathbf{v}\|_{\eta_1}} \geq \max_{\dim(U)=n} \min_{\mathbf{v} \in U} \frac{\langle A\mathbf{v}, \mathbf{v} \rangle}{\|\mathbf{v}\|_{\eta_2}} = \tau_n(\eta_2),$$

for any $n \in \mathbb{N}$. □

4. Interpretation of the results and imaging method

This Section provides a discussion on the impact of the previous results. Specifically, we discuss the relevance of the completeness and orthogonality of the basis $\{\mathbf{j}_n\}_{n \in \mathbb{N}}$ and the foundation of the imaging method based on MP.

4.1. The Completeness of the basis

The sequence $\{\mathbf{j}_n\}_{n \in \mathbb{N}}$ forms a complete basis in $H_L(\Omega)$, as proved in (2.1). Furthermore, we show that any $\mathbf{J} \in L^2(0, T; H_L(\Omega))$ can be represented by means of the following Fourier series:

$$\mathbf{J}(x, t) = \sum_{n=1}^{\infty} i_n(t) \mathbf{j}_n(x) \quad \text{in } \Omega \times [0, T]. \quad (4.1)$$

Moreover, when T is finite, it is possible to prove that [1]:

$$L^2(0, T; H_L(\Omega)) = \overline{L^2(0, T) \otimes H_L(\Omega)}.$$

Function i_n can be found by solving an ordinary differential equation:

$$r_n i_n + l_n i_n' = \mathcal{E}_n \quad \forall n \in \mathbb{N}, \quad (4.2)$$

where $r_n = \langle \eta \mathbf{j}_n, \mathbf{j}_n \rangle$, $l_n = \langle A \mathbf{j}_n, \mathbf{j}_n \rangle$ and $\mathcal{E}_n = -\langle \partial_t \mathbf{A}_S, \mathbf{j}_n \rangle$.

Moreover, when the source current \mathbf{J}_s is either vanishing or constant in time, we have $\mathcal{E}_n = 0$ for any $t > 0$ and, hence:

$$i_n(t) = i_n(0) e^{-t/\tau_n(\eta)}, \quad (4.3)$$

where we exploited $l_n/r_n = \tau_n(\eta)$. Equation (4.3), together with (4.1), gives (1.2).

4.2. Monotonicity, Shape Reconstruction, and Bounds

The inverse obstacle problem is one of the more important application of MP. In this framework, the unknown is the shape of one (or more) inclusions in a background medium. Let η_{BG} be the electrical resistivity of the background medium and let η_I be the electrical resistivity of inclusions. For the sake of simplicity, we assume that both η_{BG} and η_I are constant, but this assumption can be relaxed. In addition, we assume $\eta_I > \eta_{BG}$; the other case ($\eta_I < \eta_{BG}$) can be treated similarly.

If A is the region occupied by an inclusion, the related electrical resistivity is $\eta_A(x) = \eta_I \chi_A(x) + \eta_{BG} \chi_{\Omega \setminus A}(x)$ in Ω . Then, Theorem 3.3 implies the following form of MP:

$$A \subset B \subset \Omega \implies \tau_n(B) \leq \tau_n(A) \quad \forall n \in \mathbb{N}. \quad (4.4)$$

An imaging algorithm could be based on the equation (4.4) and, under proper conditions, upper and lower bounds are available, even in the presence of noise (see [10], based on [7, 30]). That is, if $V \subset \Omega$ is an inclusion to be retrieved starting from the knowledge of the time constants, the MP algorithm provides two subsets V^I and V^U such that $V^I \subseteq V \subseteq V^U$.

More precisely, the imaging algorithm is based on the following proposition:

$$\exists m \in \mathbb{N} : \tau_m(B) > \tau_m(A) \implies A \not\subseteq B, \quad (4.5)$$

which is an equivalent form of (4.4).

Starting from (4.5) we have the following imaging method (Union based):

$$V^U = \bigcup_{k \in S^U} \{T_k^U : \tau_n(V) \leq \tau_n(T_k^U) \quad \forall n \in \mathbb{N}\}, \quad (4.6)$$

where the T_k^U s are “test” domains forms a covering of the region of interest (ROI) and S^U is a proper set of indices. In this reconstruction rule we search for those test domains T_k^U which are seen as included in V , when analyzed from the time constants perspective.

A second option is given by the following reconstruction rule (Intersection based):

$$V^I = \bigcap_{k \in S^I} \{T_k^I : \tau_n(T_k^I) \leq \tau_n(V) \quad \forall n \in \mathbb{N}\}. \quad (4.7)$$

In this reconstruction rule we search for those test domains T_k^I which are seen as including V , when analyzed from the time constants perspective.

A third option is given by

$$V^{SU} = V_a^U \cap V_b^U \quad (4.8)$$

where V_a^U and V_b^U are union based reconstructions, but related to two different families of tests domains: $\{T_k^a\}_{k \in S^a}$ and $\{T_k^b\}_{k \in S^b}$. In this reconstruction rule, we first evaluate two upper bounds V_a^U and V_b^U to the unknown defect V and, then, we compute their intersection to reduce the test domains erroneously included in the two partial reconstructions.

5. Numerical Examples

In this section, a few numerical examples will be presented to demonstrate the MP of time constants in eddy current testing and its application in tomography. These examples are reproduced from [2, 3, 4] and they have been prepared with an in-house numerical model as described in [31]. The time constants for a given configuration are always arranged in the descending order.

5.1. Evidence of the Monotonicity Principle

The first numerical example proves the MP (see [3] for details). The background domain is a conductive slab which consists of $10 \times 10 \times 4$ voxels. The electric conductivity of the defects is significantly smaller than that of the background.

Figure 2(a) shows defect D_α , made by $2 \times 2 \times 1$ voxels and defect D_β , made by $4 \times 4 \times 1$ voxels, being D_α completely enclosed by D_β . As expected, the difference of the corresponding time constants $\tau_i(D_\alpha) - \tau_i(D_\beta)$ is non-negative for all values of i . Figure 2(b) illustrates a case where the defects are partially overlapped. Specifically, D_α is made by $4 \times 4 \times 2$ voxels, whereas defect D_β is made by $6 \times 6 \times 1$ voxels. In this case the difference $\tau_i(D_\alpha) - \tau_i(D_\beta)$ presents non permanence of the sign, as showed in Figure 2(b).

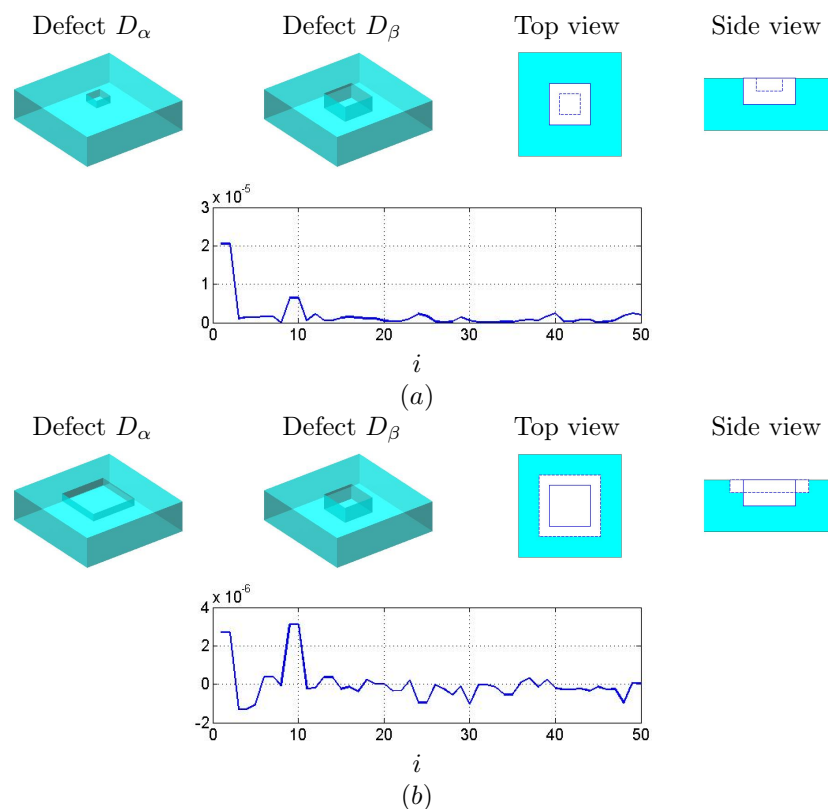


Figure 2. Schematic of the slab and defects. and plot of $\tau_i(D_\alpha) - \tau_i(D_\beta)$ for the first 50 time constants. (a) Defect D_α is enclosed by D_β . (b) Defects D_α and D_β are partially overlapped. This Figure is reproduced from [3] with the kind permission of IOS Press.

5.2. The modes

In this second example we investigated how defects impact time constants. Let us consider a simple test case, a conductive cube of $20 \text{ mm} \times 20 \text{ mm} \times 20 \text{ mm}$. The electrical resistivity of the cube is $1 \times 10^{-7} \Omega \text{ m}$. By solving the generalized eigenvalue problem (2.4), we obtain the time constants τ_i and the associated natural modes \mathbf{j}_i . Figure 3 plots the natural modes in terms of \mathbf{j}_i for some selected i . The eddy currents related to the 1st, 2nd and 3rd time constants circulate mainly on the surfaces of the cube. These three modes are equivalent up to a proper rotation as they represent multiplicative eigenvalues in (2.4). Similarly, other groups of equivalent modes are $\{4, 5\}$, $\{6, 7, 8\}$ and $\{9, 10, 11\}$. The natural modes in the same group share identical time constants.

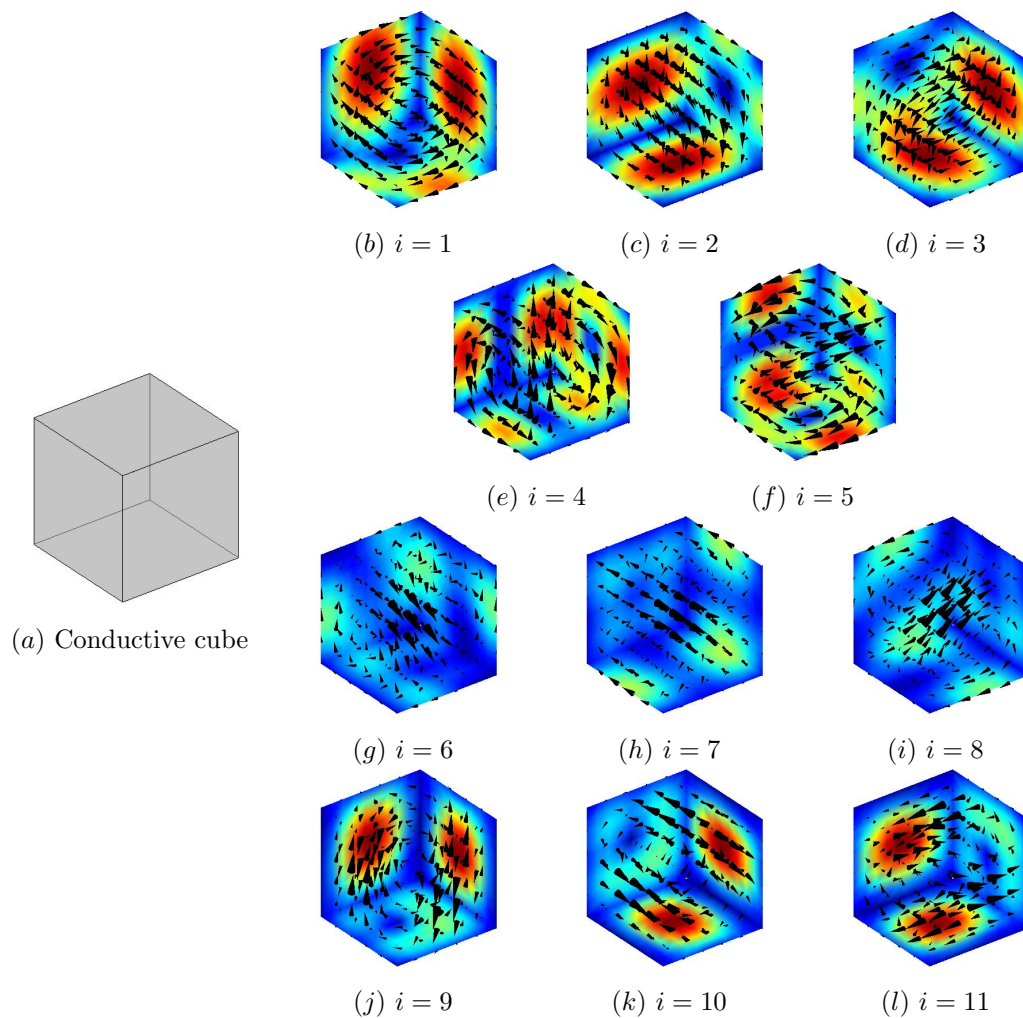
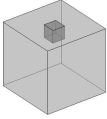


Figure 3. The natural modes of a conductive cube. (a) The cube, and (b)-(l) the natural modes associated with the 1st to 11th time constants. This Figure is reproduced from [2] with the kind permission of Institute of Physics (IOP).

When there is a defect in the cube, the eddy current is forced to redistribute around the defect. The defect impacts a mode if and only if it interacts significantly with the associated eddy current. For instance, if a defect is located in the center of the cube, it will barely make any impact to the modes that circulate mainly on the surface, e.g. the 1st, 2nd and 3rd mode. On the other hand, the same defect completely blocks the path of the 6th, 7th and 8th mode, modifying the corresponding time constants.

As a comparison, a surface breaking defect on the top surface and a buried defect in the center of the specimen were considered, and the time constants were computed with and without the defect. The dimensions of the defects are $4 \text{ mm} \times 4 \text{ mm} \times 4 \text{ mm}$. The surface breaking defect causes significant changes in the time constants of modes $i = 2, 3$ and $i = 10, 11$ as it blocks the current of these modes; the buried defect instead causes changes in the time constants of modes $i = 6, 7, 8$. The corresponding results are summarized in Table 1 and Table 2.

Table 1. The perturbation of time constants when introducing a surface breaking defect. This Table is reproduced from [2] with the kind permission of Institute of Physics (IOP).

defect	No. No defect (μs)	With defect (μs)	Difference (μs)	
	1	178	178	0
	2	178	172	6
	3	178	172	6
	4	96.2	96.0	0.2
	5	96.2	96.0	0.2
	6	89.8	89.6	0.2
	7	89.8	89.6	0.2
	8	89.8	88.4	1.4
	9	78.2	77.9	0.3
	10	78.2	74.2	4
	11	78.2	74.2	4

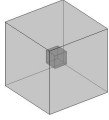
From these simple test cases, we notice that the time constants are sensitive to buried defects if their associated modes redistribute and change their paths due to this defect. Therefore, the analysis of time constants, especially whose natural modes have strong currents in the center part, is a valuable tool for inspecting the innermost regions of the specimen, which is usually a difficult task with conventional eddy current methods.

5.3. The role of the symmetry

Time constants from two configurations that are equal apart from an isometric transformation of the space are identical. Therefore, it is impossible to distinguish two defects that are equal apart from an isometry. In this section, we investigate this aspect and suggest the use of additional conductors to break the symmetry.

Let us consider a pipe, which is commonly used in many industrial applications, e.g. oil/gas transmission, steam generation in power plants, as our subject of inspection

Table 2. The perturbation of time constants when introducing a buried defect. This Table is reproduced from [2] with the kind permission of Institute of Physics (IOP).

defect	No.	No defect (μs)	With defect (μs)	Difference (μs)
	1	178	177	1
	2	178	177	1
	3	178	177	1
	4	96.2	96.2	0
	5	96.2	96.2	0
	6	89.8	81.6	8.2
	7	89.8	81.6	8.2
	8	89.8	81.6	8.2
	9	78.2	78.2	0
	10	78.2	78.2	0
	11	78.2	78.2	0

(Figure 4). The inner and outer radii of the pipe are 5 mm and 9 mm, respectively. We consider only a section of the pipe which is 10 mm long. For numerical simulations, this cylinder domain is meshed into hexahedral elements with 10 uniformly distributed elements in axial direction, 10 uniformly distributed elements in radial direction and 30 uniformly distributed elements in azimuthal direction. Multiple coils are used to pick up signals at the inner surface of the pipe.

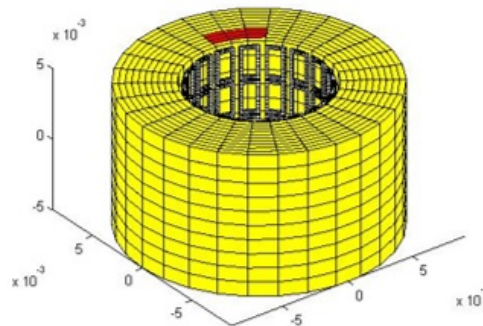


Figure 4. Mesh of the cylinder pipe and pick up coils. This Figure is reproduced from [4] with the kind permission of IOS Press.

Figure 6 highlights two symmetric defects, colored in blue and red respectively. As depicted in the figure, the corresponding time constants are identical because of the symmetry and, hence, they cannot be uniquely determined by using the MP. A possible method to overcome this problem is introducing additional pieces of conductors to break the symmetry of the underlying structure, as illustrated in green in Figure 5. These additional conducting patches are introduced nondestructively together with the

inspection system (coils). They produce perturbations in the eddy currents modes, while not changing the property of the specimen, i.e. the pipe. In order to raise significant changes to the eddy current distribution, the size of additional patches should be large enough. For instance, in this article, their sizes are about 40% of the pipe, in all dimensions.

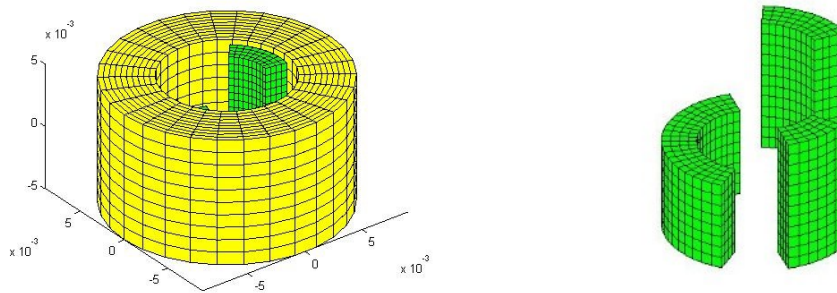
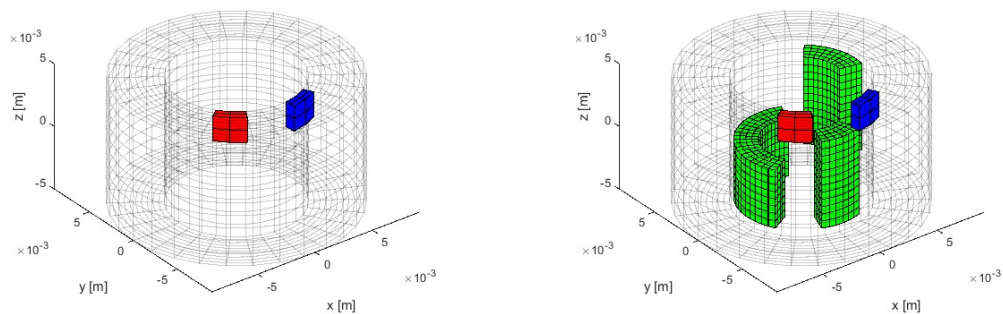


Figure 5. Additional conductor patches and their mesh together with the cylinder. This Figure is reproduced from [4] with the kind permission of IOS Press.



(a) two circular symmetrical defects

(b) defects lose symmetry with respect to extra conductor patches

Figure 6. Introducing conductor patches breaks geometrical symmetry. This Figure is reproduced from [4] with the kind permission of IOS Press.

After introducing the additional patches (Figure 5(b)) symmetric defects could be distinguished via time constants since their relative positions with respect to the additional conductors are different. Figure 7 illustrates the 11th to 20th time constants related to these two defects. In this test case, the conductivity of the background and of the additional conductors is 10^7 S/m, that of the defects is 10^5 S/m.

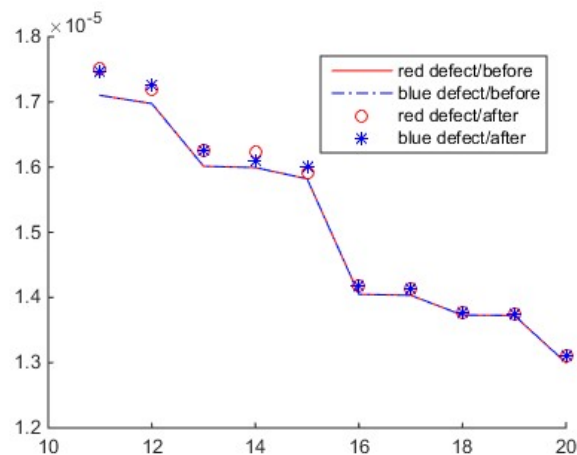


Figure 7. Time constants related to symmetrical defects before and after the introduction of the additional conductors. This Figure is reproduced from [4] with the kind permission of IOS Press.

5.4. Imaging

Following the previous example, a defect can be uniquely identified via MP after introducing the external patches. In this subsection, we test numerically the three different imaging strategies of (4.6), (4.7) and (4.8) for defects in the pipe. Two test cases are presented: a buried and centered defect and an inner-surface breaking and edged defect. Each of these defects consists of $3 \times 3 \times 3$ voxels, in the cylindrical structure.

To reconstruct these “unknown” defects, we calculate in advance the time constants for small test elements (defects made by $2 \times 2 \times 2$ voxels) and large test elements (defects made by $4 \times 4 \times 4$ voxels).

All time constants are calculated numerically and only the largest 50 time constants are used in the reconstruction algorithm. Multiplicative noise model is assumed on the measurement of the time constants related to the unknown defect V and the noise level is 0.01%, i.e. $\tilde{\tau}_i^V = \tau_i^V \cdot (1 + \xi)$, where τ_i^V is the i -th largest time constant related to V and $\tilde{\tau}_i^V$ is the noised measurement of τ_i^V , ξ is uniformly distributed in $[-0.0001, 0.0001]$.

The first test case considers a defect buried in the pipe. Imaging results are summarized in figure 8. Strategies 1 and 3 give good reconstructions, however strategy 2, not reported here, gives a void set ($V^I = \emptyset$). In fact, when applying strategy 2, there were many “false” calls, even when the real defect was not included in the test element. The intersection of these false calls gave the empty set. Also, comparing the result of strategies 1 and 3, it is worth noting that the intersection (4.8) of two upper bounds arising from (4.6) but from two families of test elements, gives a better reconstruction where some superfluous voxels are excluded.

The last test case refers to a surface breaking defect at the edge of the pipe (Figure 9). This case nicely demonstrated the role of the additional conductive patches. They helped to locate the azimuthal position of the defect, as well distinguish the defect at the upper edge from defects at the lower edge. However, we noticed that a second

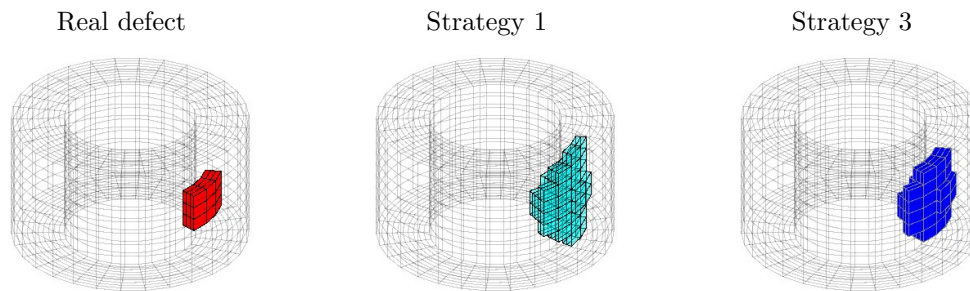


Figure 8. Reconstruction of a buried defect. This Figure is reproduced from [4] with the kind permission of IOS Press.

superfluous defect was reconstructed at the center part of the pipe.

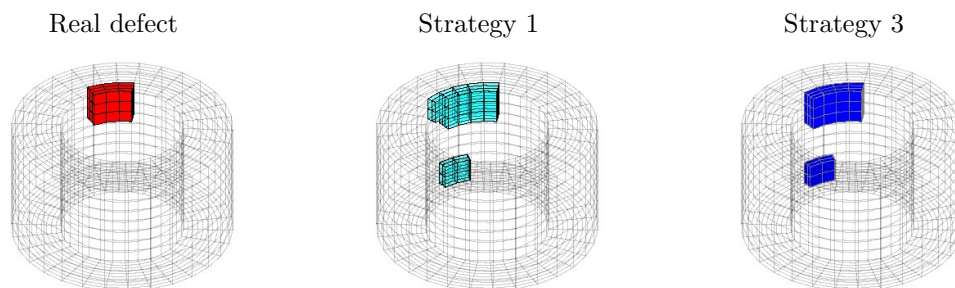


Figure 9. Reconstruction of a surface breaking defect at the edge. This Figure is reproduced from [4] with the kind permission of IOS Press.

References

- [1] Tamburrino A, Piscitelli G and Zhou Z 2021 *Inverse Problems* **37** 095003
- [2] Su Z, Ventre S, Udpa L and Tamburrino A 2017 *Inverse Problems* **33** 125007
- [3] Tamburrino A, Su Z, Lei N, Udpa L and Udpa S 2015 The monotonicity imaging method for pect *Electromagnetic Nondestructive Evaluation (XVIII)* vol 40 pp 159–166
- [4] Tamburrino A, Su Z, Ventre S, Udpa L and Udpa S 2016 Monotonicity based imaging method in time domain eddy current testing *Electromagnetic Nondestructive Evaluation (XIX)* vol 41 pp 1–8
- [5] Haus H A and Melcher J R 1989 *Electromagnetic fields and energy* vol 107 (Prentice Hall Englewood Cliffs, NJ) ISBN 9780132490207
- [6] Bossavit A 1981 *Computer methods in applied mechanics and engineering* **27** 303–318
- [7] Tamburrino A and Rubinacci G 2002 *Inverse Problems* **18** 1809–1829
- [8] Tamburrino A and Rubinacci G 2006 *IEEE Transactions on Magnetics* **42** 2017–2028
- [9] Tamburrino A 2006 *Journal of Inverse and Ill-posed Problems* **14** 633 – 642
- [10] Tamburrino A, Vento A, Ventre S and Maffucci A 2016 *Studies in Applied Electromagnetics and Mechanics* **41** 284–292
- [11] Tamburrino A, Calvano F, Ventre S and Rubinacci G 2012 *NDT and E International* **47** 26–34

- [12] Su Z, Udpa L, Giovinco G, Ventre S and Tamburrino A 2017 Monotonicity principle in pulsed eddy current testing and its application to defect sizing *2017 International Applied Computational Electromagnetics Society Symposium - Italy, ACES 2017*
- [13] Maffucci A, Vento A, Ventre S and Tamburrino A 2016 *IEEE Transactions on Components, Packaging and Manufacturing Technology* **6** 1417–1427 ISSN 2156-3985
- [14] Tamburrino A, Ventre S and Rubinacci G 2010 *Inverse Problems* **26** 074016
- [15] Soleimani M 2007 *International Journal for Information & Systems Sciences* **3** 283–291 ISSN 1708-296X
- [16] Eberle S and Harrach B 2021 *Inverse Problems* **37** 045006
- [17] Harrach B, Pohjola V and Salo M 2019 *Analysis & PDE* **12** 1741–1771
- [18] Griesmaier R and Harrach B 2018 *SIAM Journal on Applied Mathematics* **78** 2533–2557
- [19] Albicker A and Griesmaier R 2020 *Inverse Problems*
- [20] Daimon T, Furuya T and Saiin R 2020 *Inverse Problems in Science and Engineering* 1–12
- [21] Harrach B and Lin Y H 2019 *SIAM Journal on Mathematical Analysis* **51** 3092–3111
- [22] Corbo Esposito A, Faella L, Piscitelli G, Prakash R and Tamburrino A 2021 *Inverse Problems* **37**
- [23] Colton D and Kirsch A 1996 *Inverse Problems* **12** 383–393
- [24] Kirsch A 1998 *Inverse Problems* **14** 1489–1512
- [25] Ikehata M 2000 *Inverse Problems* **16** 785–793
- [26] Devaney A J 2000 Super-resolution processing of multi-static data using time reversal and music northeastern University preprint
- [27] Fernandez L, Novotny A A and Prakash R 2019 *Mathematical Methods in the Applied Sciences* **42** 2256–2278
- [28] Touzani R and Rappaz J 2014 *Mathematical Models for Eddy Currents and Magnetostatics: With Selected Applications, Scientific Computation*
- [29] Albanese R and Rubinacci G 1997 *Finite element methods for the solution of 3D eddy current problems* vol 102 (Elsevier) pp 1–86
- [30] Harrach B and Ullrich M 2015 *IEEE transactions on medical imaging* **34** 1513–1521
- [31] Morozov M, Rubinacci G, Tamburrino A and Ventre S 2006 *IEEE Transactions on Magnetics* **42** 1568–1576